
Suzaku detection of enigmatic geocoronal solar wind charge exchange event associated with coronal mass ejection

**Daiki ISHI,^{1,*} Kumi ISHIKAWA,² Masaki NUMAZAWA,¹ Yoshizumi MIYOSHI,³
Naoki TERADA,⁴ Kazuhisa MITSUDA,² Takaya OHASHI,¹ and Yuichiro
EZOE¹**

¹Tokyo Metropolitan University, 1-1 Minami-Osawa, Hachioji, Tokyo 192-0397, Japan

²Institute of Space and Astronautical Science, Japan Aerospace Exploration Agency, 3-1-1
Yoshinodai, Chuo-ku, Sagamihara, Kanagawa 252-5210, Japan

³Nagoya University, Furo-cho, Chikusa-ku, Nagoya, Aichi 464-8601, Japan

⁴Tohoku University, 6-3 Aramaki-Aza-Aoba, Aoba-ku, Sendai, Miyagi 980-8578, Japan

*E-mail: ishi-daiki@ed.tmu.ac.jp

Received 2018 May 9; Accepted 2018 November 23

Abstract

Suzaku detected an enhancement of soft X-ray background associated with solar eruptions on 2013 April 14–15. The solar eruptions were accompanied by an M6.5 solar flare and a coronal mass ejection with magnetic flux ropes. The enhanced soft X-ray background showed a slight variation in half a day and then a clear one in a few hours. The former spectrum was composed of oxygen emission lines, while the later one was characterized by a series of emission lines from highly ionized carbon to silicon. The soft X-ray enhancement originated from geocoronal solar wind charge exchange. However, there appeared to be no significant time correlation with the solar wind proton flux measured by the ACE and WIND satellites. From other solar wind signatures, we considered that an interplanetary shock associated with the coronal mass ejection and a turbulent sheath immediately behind the shock compressed the ambient solar wind ions and then resulted in the soft X-ray enhancement. Furthermore, the enriched emission lines were presumed to be due to an unusual set of ion abundances and

ionization states within the coronal mass ejection. We found a better time correlation with the solar wind alpha flux rather than the solar wind proton flux. Our results suggest that the solar wind proton flux is not always a good indicator of geocoronal solar wind charge exchange, especially associated with coronal mass ejections. Instead, the solar wind alpha flux should be investigated when such a soft X-ray enhancement is detected in astronomical observations.

Key words: Earth — Sun: flares — Sun: coronal mass ejections (CMEs) — Sun: solar-terrestrial relations — X-rays: diffuse background

1 Introduction

Solar eruptions such as solar flares and coronal mass ejections (CMEs) are powerful explosive phenomena in our solar system. Solar flares, intense bursts of radiation across the entire electromagnetic spectrum ranging from radio waves to γ -rays, release more than 10^{32} erg of magnetic energy in tens of minutes (e.g., Priest & Forbes 2002). The CMEs are huge clouds of coronal magnetized plasma with a typical mass of 10^{15-16} g and speeds of 250–1000 km s⁻¹ into interplanetary space (Webb & Howard 2012). These eruptions are more frequent during the active phase of the solar cycle and have a significant influence on planetary atmospheres and their surrounding environments.

Solar activity influences X-ray astronomical observations by spacecrafts. The spacecrafts often detect increased background X-rays when their lines of sight directions face on the sunlit side of the Earth's atmosphere (e.g., McKenzie et al. 1982). X-rays from the sunlit atmosphere are due to Thomson scattering of solar X-rays by electrons in atmospheric atoms and molecules, as well as absorption of incident solar X-rays followed by the emission of characteristic K lines of atmospheric neutrals. These background X-rays are usually removed by discarding time intervals when the line of sight direction faces on the sunlit atmosphere.

The other important background source is solar wind charge exchange (SWCX) in the Earth's exosphere or geocoronal SWCX. A highly charged ion in the solar wind strips an electron from an exospheric neutral atom or molecule, and then releases X-ray or ultraviolet photons when the electron cascades into the ground state. The most explicit signs of the geocoronal SWCX were discovered during the ROSAT All Sky Survey (e.g., Snowden et al. 1994; Cravens et al. 2001). Thanks to recent X-ray astronomical observations with X-ray CCDs onboard Chandra, XMM-Newton, and Suzaku (e.g., Snowden et al. 2004; Wargelin et al. 2004; Fujimoto et al. 2007; Carter & Sembay 2008; Ezoe et al. 2010; Ezoe et al. 2011; Ishikawa et al. 2013), the geocoronal SWCX are now established as time

variable diffuse background. Careful checks of background X-rays combined with simultaneously observed solar wind data are essential for removing the geocoronal SWCX.

Geocoronal SWCX provides not only background signals but also important information such as the exospheric density and the minor constituents of the solar wind. Models to simulate the spatial distribution of the geocoronal SWCX (e.g., Robertson et al. 2006) indicated that the distribution is non-uniform and higher at the dayside of the Earth’s magnetosphere, especially the magnetosheath and the magnetosheric cusps.

Carter & Sembay (2008) and Carter et al. (2011) systematically searched for geocoronal SWCX emission from XMM-Newton archival data. Most of the observations affected by the geocoronal SWCX were found through the sub-solar side of the magnetosheath. The strong SWCX emission was sometimes observed even when the line of sight direction did not intersect the magnetosheath. They mentioned that the latter cases probably originated from non-geocoronal SWCX in the heliosphere (e.g., Cravens 2000; Koutroumpa et al. 2007). Carter et al. (2010) argued that the most spectrally rich case was attributed to a CME passing through the Earth on 2001 October 21.

The X-ray Imaging Spectrometer (XIS) onboard Suzaku consists of three front-illuminated (FI) CCDs and one back-illuminated (BI) CCD and has a good energy response and a low background rate (Mitsuda et al. 2007; Koyama et al. 2007). Fujimoto et al. (2007) and Ezoe et al. (2011) discovered geocoronal SWCX events in the directions of the magnetospheric cusps, while Ezoe et al. (2010) found an event toward the sub-solar side of the magnetosheath. Ishikawa et al. (2013) detected one of the strongest geocoronal SWCX emission when the line of sight direction faced on the anti-sunward side of the magnetosheath. These events showed a significant correlation of the X-ray flux with the simultaneously observed solar wind proton and ion fluxes.

Motivated by these Suzaku detections and their correlations with the solar wind data, we are proceeding a systematic search for the geocoronal SWCX events from all the Suzaku archival data. During this systematic search, we found a distinctive geocoronal SWCX event most probably associated with an M6.5 solar flare and a CME recorded on 2013 April 11. This event could be missed in the standard search for the geocoronal SWCX events using a time correlation with the solar wind proton flux. In this paper, we describe characteristics of this geocoronal SWCX event.

2 Observation

Suzaku observed a supernova remnant (SNR) 0509–67.5 in the Large Magellanic Cloud (LMC) on 2013 April 11–15 (ObsID: 508072010). The pointing center was $(\text{RA}, \text{Dec})_{\text{J2000.0}} = (77^\circ 393, -67^\circ 525)$, which corresponds to $(l, b) = (278^\circ 147, -34^\circ 586)$ in Galactic coordinates. This SNR has

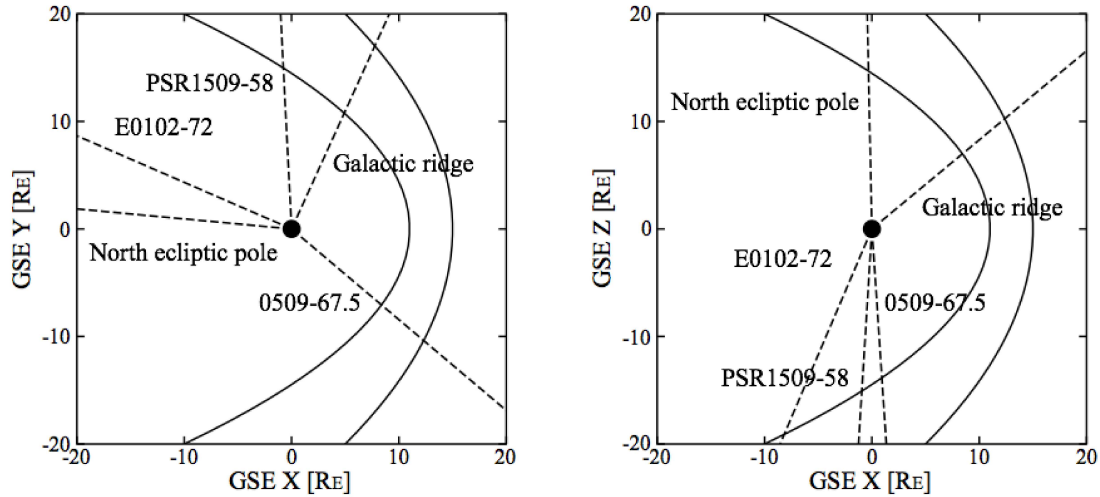


Fig. 1. Average lines of sight directions in the GSE XY and XZ planes during this observation (0509–67.5), the north ecliptic pole (Fujimoto et al. 2007), the galactic ridge (Ezoe et al. 2010), PSR B1509–58 (Ezoe et al. 2011), and 1E 0102.2–7219 (Ishikawa et al. 2013). Filled black circles in each panels represent Earth. Two solid curves indicate approximate positions of the Earth’s magnetopause and bow shock.

a shell-like structure extending to the angular radius of $14''.8$ in the X-ray band (Warren & Hughes 2004). Its X-ray spectrum consists of a non-thermal continuum component and many bright emission lines originating from thermal plasma such as silicon, sulfur, and iron. Yamaguchi et al. (2014) analyzed all extant Suzaku data including this observation and constrained their progenitor types.

We utilized the same data for an investigation of the geocoronal SWCX emission. Figure 1 shows the average line of sight direction in Geocentric Solar Ecliptic (GSE) coordinates during this observation. A normalized pointing vector in GSE coordinates was $(0.0668, -0.0564, -0.9958)$. It passed through the southern magnetospheric cusp where stronger SWCX flux would be expected from the past Suzaku observation of the geocoronal SWCX event on 2005 August 23–24 (Ezoe et al. 2011). This observation covered from 2013 April 11, 01:26 to April 15, 03:01 UT (Day of Year, DOY, 101.06–105.13 in 2013).

We started data analyses from cleaned event data that had already been pre-processed with the standard screening criteria.¹ Its processing version was 3.0.22.44. The standard screening removes high-background events mainly during passages through the South Atlantic Anomaly, and selects good time intervals when the satellite can stably point at the astronomical source without the Earth occultation. We utilized the HEASoft version 6.21 package to handle scientific products and instrumental response files. The XIS2 turned off due to damages by a micro-meteorite on 2006 November

¹ <https://heasarc.gsfc.nasa.gov/docs/suzaku/analysis/abc/abc.html>.

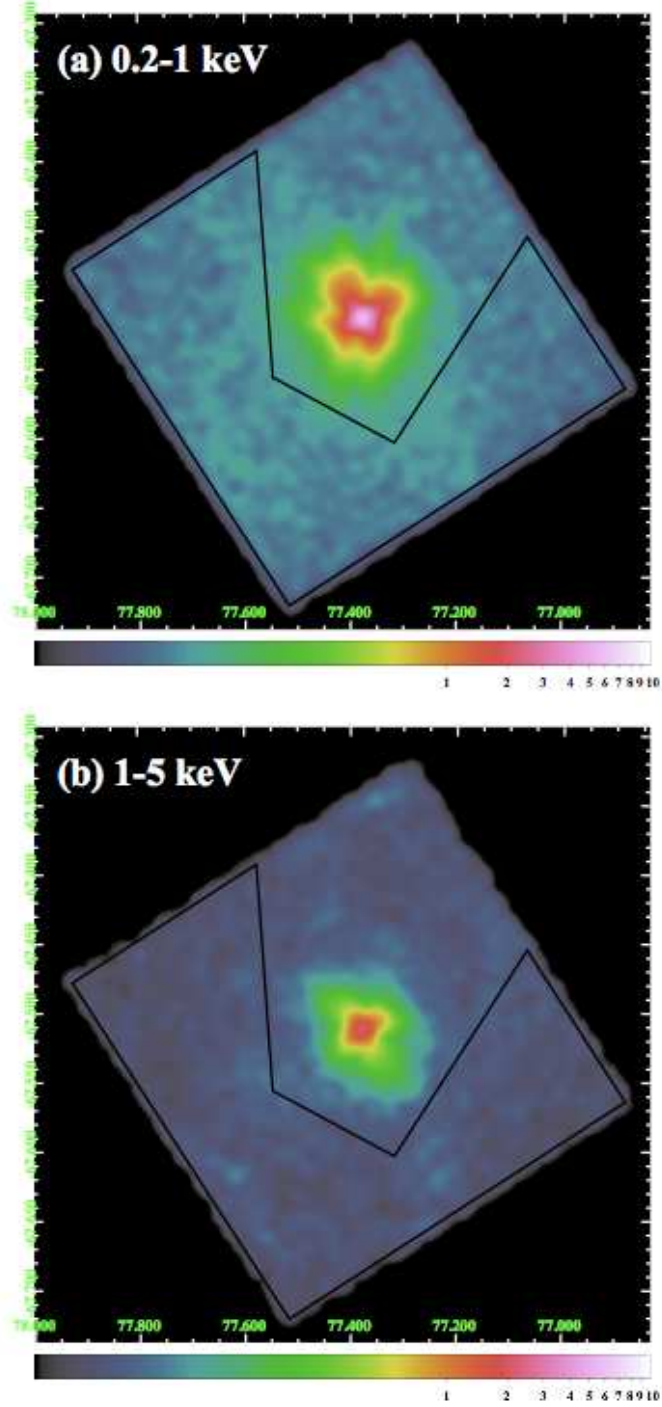


Fig. 2. XIS images in (a) 0.2–1 keV (XIS1) and (b) 1–5 keV (XIS3) displayed on J2000.0 coordinates. For clarity, the images were smoothed by a Gaussian profile of $\sigma = 15$ pixels corresponding to $\sim 15''$. A color scale refers to counts per pixel. The polygon region is used for light curve and spectral analyses.

9.² The XIS0 was also damaged by a similar accident on 2009 June 23.³ Hence, we used only XIS1 and 3 data in this paper. The XIS1 has higher sensitivity to soft X-rays because it is a BI-type CCD and the XIS3 is a FI-type one. Figure 2 shows XIS images in two representative energy bands. To minimize contamination from the X-ray emission of the main target located at the center of the field of view, we defined a polygon region and called it a terrestrial diffuse X-ray (TDX) region whose total area is 175.1 arcmin².

An additional screening was necessary for the cleaned data so as to avoid contamination by scattering of solar X-rays from the Earth’s atmosphere (e.g., Ezoe et al. 2011; Sekiya et al. 2014). We found neutral nitrogen and oxygen emission lines in the TDX spectrum when the elevation angle from the Earth rim (ELV) was 5°–10°, and then screened the data with the ELV >10° criteria. After this screening, these emission lines were negligible and an effective exposure time was 157.4 ks.

3 Light Curve

We first extracted X-ray light curves from the TDX region in the 0.5–0.7 and 2.5–5 keV bands as shown in figure 3. These light curves are binned with a time bin of 4096 s. The soft X-ray band could be affected by oxygen emission lines often seen in the geocoronal SWCX events, while the harder one is almost composed of a non-SWCX continuum. The 0.5–0.7 keV count rate shows a sudden enhancement just before the end of this observation. Furthermore, there slightly appears to be an increase before the sudden enhancement. Hereafter, we define the “stable” period as DOY 101.06–103.89, the “pre-flare” period as DOY 103.98–104.71, and the “flare” period as DOY 104.78–105.07. The average rate in the “stable” period is 0.033 ± 0.006 cts s^{−1}, while those in the “pre-flare” and “flare” periods are 0.039 ± 0.005 and 0.061 ± 0.013 cts s^{−1}, respectively. Errors are 1 σ significance. The count rate increased slightly during the “pre-flare” period and by a factor of ~ 2 from the “stable” period to the “flare” period. In contrast, the 2.5–5 keV count rate shows less variability with the average rates of 0.015 ± 0.003 cts s^{−1} in the “stable” period, 0.015 ± 0.004 cts s^{−1} in the “pre-flare” period, and 0.014 ± 0.002 cts s^{−1} in the “flare” period.

We then plotted four solar wind parameters: the solar wind proton flux, the interplanetary magnetic field (IMF) frozen-in the solar wind plasma, the solar wind proton temperature, and the solar wind plasma beta (the ratio of plasma to magnetic pressure). These parameters were taken from high-resolution OMNI data time-shifted to the Earth’s bow shock nose.⁴ The solar wind proton

² <http://www.astro.isas.jaxa.jp/suzaku/news/2006/1123/>.

³ <http://www.astro.isas.jaxa.jp/suzaku/news/2009/0702/>.

⁴ https://omniweb.gsfc.nasa.gov/ow_min.html.

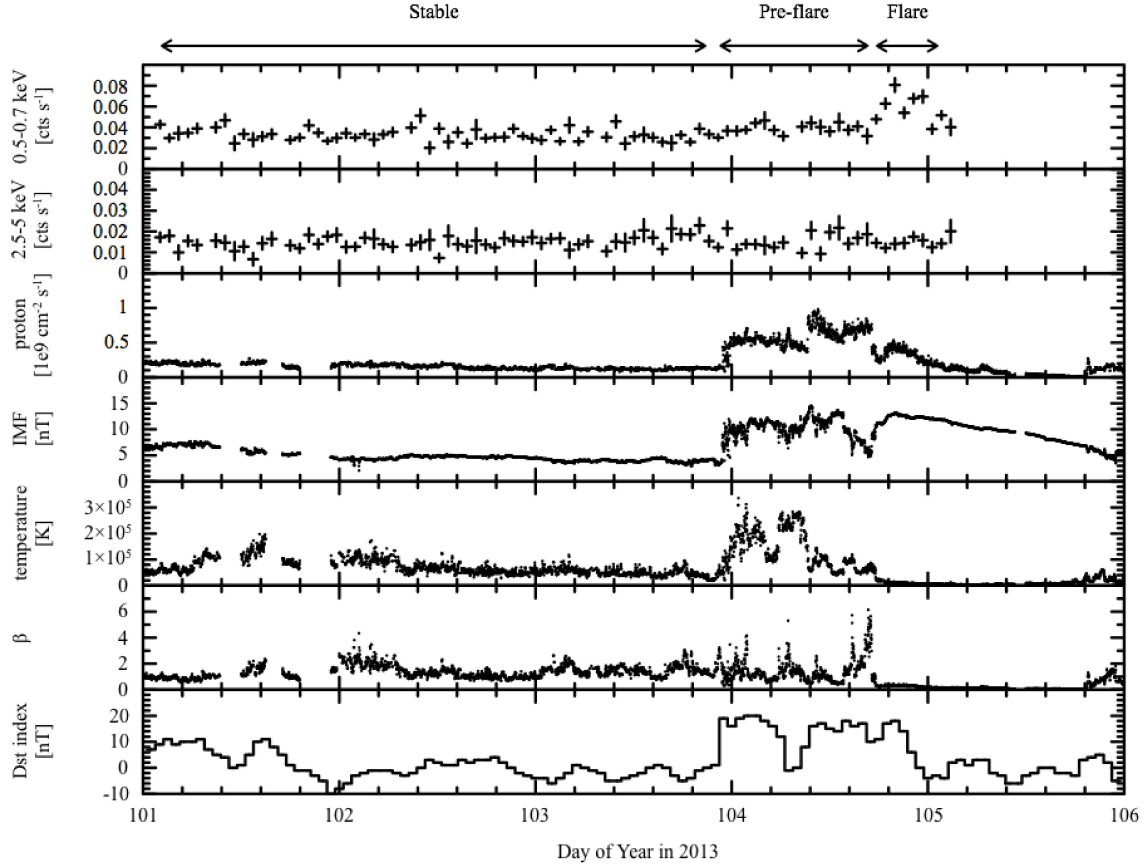


Fig. 3. XIS light curves in 0.5–0.7 keV (XIS1) and 2.5–5 keV (XIS3), solar wind proton flux, interplanetary magnetic fields frozen-in solar wind plasma, solar wind proton temperatures, solar wind plasma beta, and Dst index as function of DOY in 2013. The vertical errors are 1σ significance. The sole wind parameters were taken from the high-resolution OMNI data time-shifted to the Earth's bow shock nose. The Dst index was taken from the World Data Center for Geomagnetism, Kyoto.

flux suddenly increases just before DOY 104, and gradually decreases around DOY 104.8. The IMF exhibits two features in response to the sudden increase and the gradual decrease. One is the intense fluctuation of enhanced magnetic fields between DOY 104 and 104.7. The other is the strong and smooth magnetic field after DOY 104.8. The solar wind proton temperature also rises up with the discontinuous change in the solar wind proton flux, and then becomes extremely low at the same time as the solar wind plasma beta is largely depressed. These solar wind signatures are suggestive of a CME-induced interplanetary shock and the passage of a magnetic cloud that is a subset of CMEs.

Magnetic clouds are well defined observationally as an interplanetary structure possessing the following characteristics: enhanced magnetic fields that smoothly rotate, low proton temperatures, and low plasma beta (e.g., Burlaga et al. 1981; Zurbuchen & Richardson 2006). An M6.5 solar flare

was recorded on April 11, 06:55 UT (DOY 101.29). The CME was almost simultaneously erupted with a fast speed of $\sim 800 \text{ km s}^{-1}$. The ejected CME drove an interplanetary shock and formed a turbulent sheath immediately behind the shock. Highly compressed solar wind in the turbulent sheath results in the discontinuous change and the subsequent fluctuation just before DOY 104. More subsequently, the CME or the magnetic cloud arrived at Earth around DOY 104.8.

We also plotted hourly averages of the Dst index provided by the World Data Center for Geomagnetism, Kyoto, Japan.⁵ The Dst index is a measure of geomagnetic disturbances based on averaging the horizontal geomagnetic component from mid-latitude and equatorial magnetometer data. Negative values of the Dst index indicate that a geomagnetic storm is in progress with the growth of magnetospheric ring current (e.g., Gonzalez et al. 1994; Miyoshi & Kataoka 2005). Such negative values are seeable when the IMF remains southward directions for a prolonged time. However, the IMF was northward within the magnetic cloud and there were no dramatic decreases of the Dst index during this observation. Instead, the Dst index shows positive values after the arrival of the CME-induced interplanetary shock and the passage of the turbulent sheath. These positive values result from compression of the magnetosphere and the consequent approach of magnetopause current.

From comparison between the X-ray light curve and the solar wind parameters, the X-ray enhancement in the “pre-flare” and “flare” periods should be closely related to the passage of the turbulent sheath associated with the CME-induced interplanetary shock and the arrival of the CME. The solar wind proton flux in the “pre-flare” period is higher than that in the “flare” period. However, the X-ray enhancement in the “pre-flare” period is less remarkable than that in the “flare” period. Therefore, a correlation analysis between the X-ray light curve and the solar wind proton flux would miss the geocoronal SWCX events such as this one.

To check another possibility, i.e., whether the X-ray enhancement arises from leaked photons of the bright X-ray source and/or time variability of any other point sources, we compared images of the “pre-flare” and “flare” periods with that of the “stable” period. Figure 4 shows ratio maps produced by dividing the “pre-flare” and “flare” periods by the “stable” period in the 0.5–0.7 keV band. The ratio of the TDX region increases slightly in the “pre-flare” period and by a factor of ~ 2 in the “flare” period. In contrast, the central bright X-ray source is rather steady. Hence, the leaked photons are negligible in the TDX region. The time variability of any other point sources also contributes little to the increased ratio in the entire of the TDX region. Figure 5 shows ratio maps in the 2.5–5 keV band. The entire of the TDX region is almost steady during the “pre-flare” and “flare” periods.

⁵ (<http://wdc.kugi.kyoto-u.ac.jp/dstae/index.html>).

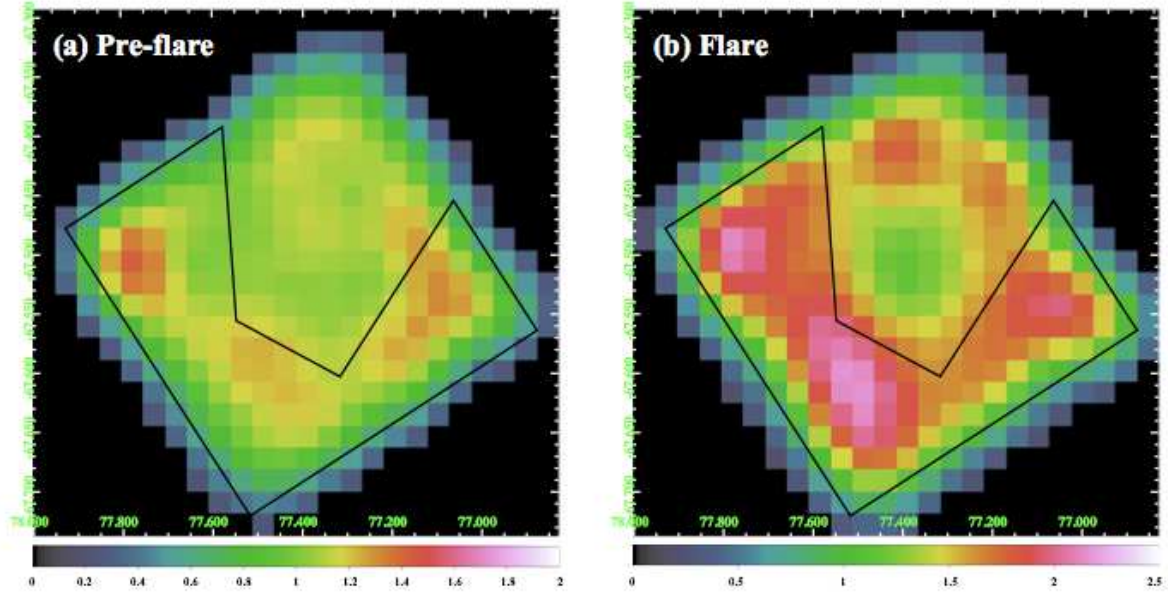


Fig. 4. XIS1 0.5–0.7 keV ratio maps in the (a) “pre-flare” and (b) “flare” periods. Each images are divided by that in the “stable” period. The difference of exposure times is corrected. For clarity, the images are binned by 64 pixels. The color scale refers to the ratio. The polygon region marks the TDX region.

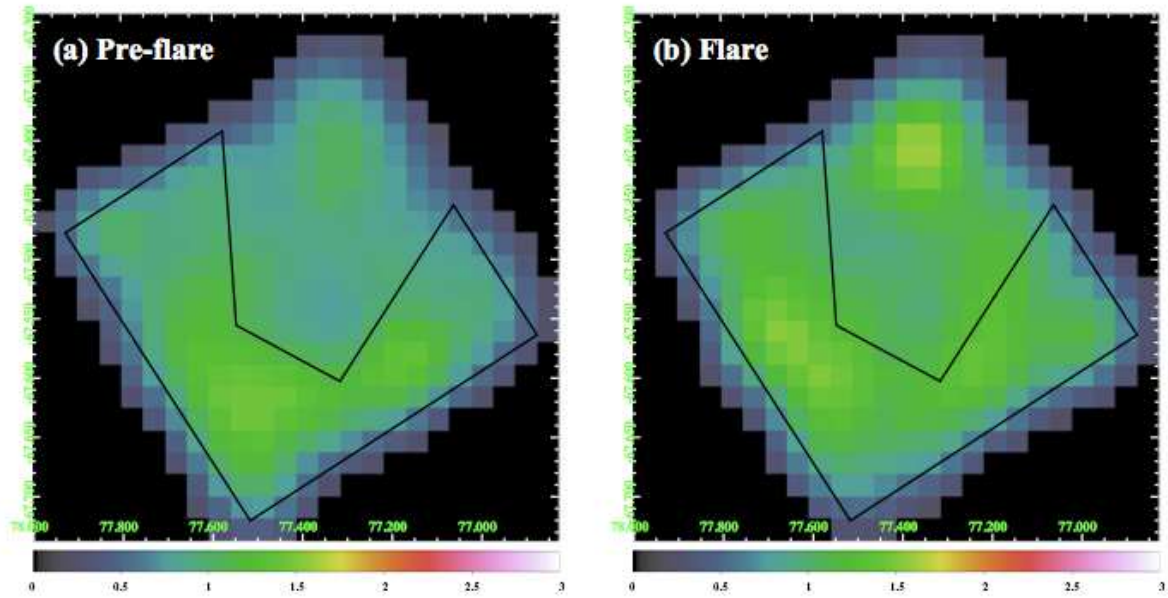


Fig. 5. XIS3 2.5–5 keV ratio maps in the (a) “pre-flare” and (b) “flare” periods. Manners are the same as in figure 4.

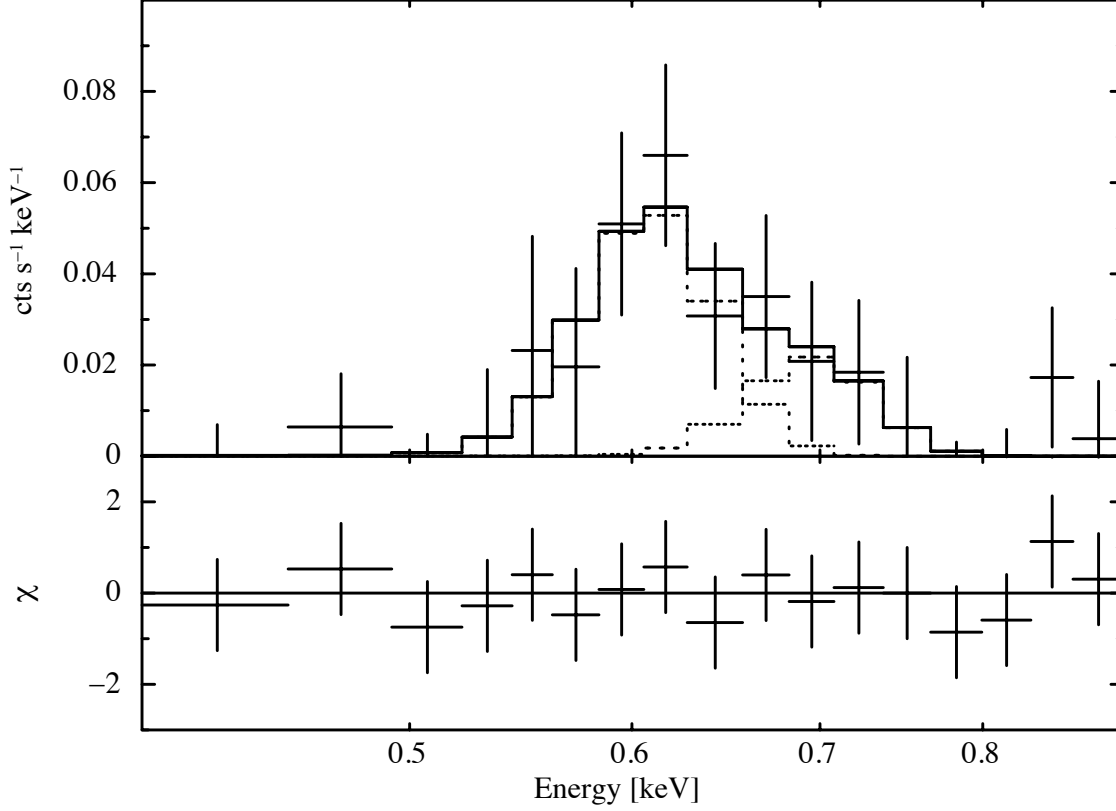


Fig. 6. XIS1 spectrum in the “pre-flare” period. The “stable” spectrum is subtracted as a background. The two Gaussian model is used and their parameters are listed in table 1.

4 Spectrum

The majority of SWCX emission lines have been found in the soft X-ray band below 2 keV, where the BI-type CCD has higher sensitivity than the FI-type one. We thus focused on the XIS1 spectra extracted from the TDX region during the “stable”, “pre-flare”, and “flare” periods. These spectra included the instrument and sky backgrounds. The instrumental background rate was almost constant due to the low-Earth orbit. The sky background originates from diffuse galactic and extragalactic emission and its spectral feature does not vary temporally. Therefore, we assumed the background spectra as constant components during this observation in the same way as Ezoe et al. (2011).

Figure 5 shows the spectrum produced by subtracting the “stable” period from the “pre-flare” period. The spectrum represents a spectral change during the “pre-flare” period. The data was modeled with two narrow Gaussians. These parameters are summarized in table 1. The line center ener-

Table 1. Result of two Gaussian fits to the spectrum shown in figure 6.*

Model	E_c^\dagger	Normalization ‡	f_X^\S	Line identification
1	608 ± 18 eV	$6.6^{+3.0}_{-2.5}$	9.6×10^{-14}	O VII (f 561 eV, i 569 eV, r 574 eV) $^{\parallel}$
2	694^{+45}_{-52} eV	1.8 ± 1.5	2.9×10^{-14}	O VIII (653 eV)
$\chi^2/\text{d.o.f}$	4.78/13			

* All the line widths are fixed at 0 eV.

$^\dagger E_c$ is the line center energy.

‡ Normalization is in units of photons $\text{s}^{-1} \text{cm}^{-2} \text{str}^{-1}$.

$^\S f_X$ is the energy flux in $\text{erg s}^{-1} \text{cm}^{-2}$.

$^{\parallel}$ f, i, and r denote forbidden, intercombination, and resonance lines.

gies were consistent with oxygen emission lines (0.5–0.7 keV) often seen in the typical geocoronal SWCX spectra. This indicates that highly ionized oxygen within the ambient solar wind increases in the turbulent sheath and then produces the geocoronal SWCX emission.

We then subtracted the spectrum of the “stable” period from that of the “flare” period. Figure 7 shows the spectrum after this subtraction. The spectrum clearly contained prominent oxygen emission lines and some excess emission lines above 0.7 keV. A series of the excess emission lines are constituted by enriched solar wind minor ions such as neon, magnesium, and silicon.

For the emission lines from highly ionized carbon, nitrogen, and oxygen, we used a theoretical SWCX emission-line model constructed by Bodewits et al. (2007). This model shows the relative emission cross-sections of highly charged ions (C V, C VI, N VI, N VII, O VII, and O VIII) in collision with atomic hydrogen for several solar wind velocities. We utilized the values for the velocity of 400 km s^{-1} , which was close to the average velocity of $\sim 450 \text{ km s}^{-1}$ during the “flare” period. The normalization of the principal transitions from each ion was fitted as a free parameter, whereas those of the minor transitions were fixed with respect to each principal transition.

The best-fit parameters are summarized in table 2. Similar to Ezoe et al. (2011), we added an extra Gaussian to reproduce the lowest energy emission line around 0.25 keV. At higher energies than the oxygen emission lines, we also added fourteen narrow Gaussians detected by Carter et al. (2010). The normalizations of C V, N VI, Fe XVII, Fe XVIII, and Fe XX were zero and negligible. We thus excluded these transitions from the best-fit parameters.

The number of the detected emission lines was one of the richest case in the past geocoronal SWCX events. We succeeded in detecting the various emission lines from highly ionized carbon to silicon. Figure 8 shows the energy flux ratios of the SWCX ion lines to the O VIII line in comparison with the XMM-Newton observation of the CME-induced geocoronal SWCX event reported by Carter et al. (2010), which was another case consisting rich emission lines. The ion composition during this observation showed the same tendency of the XMM-Newton observation. This supports that the

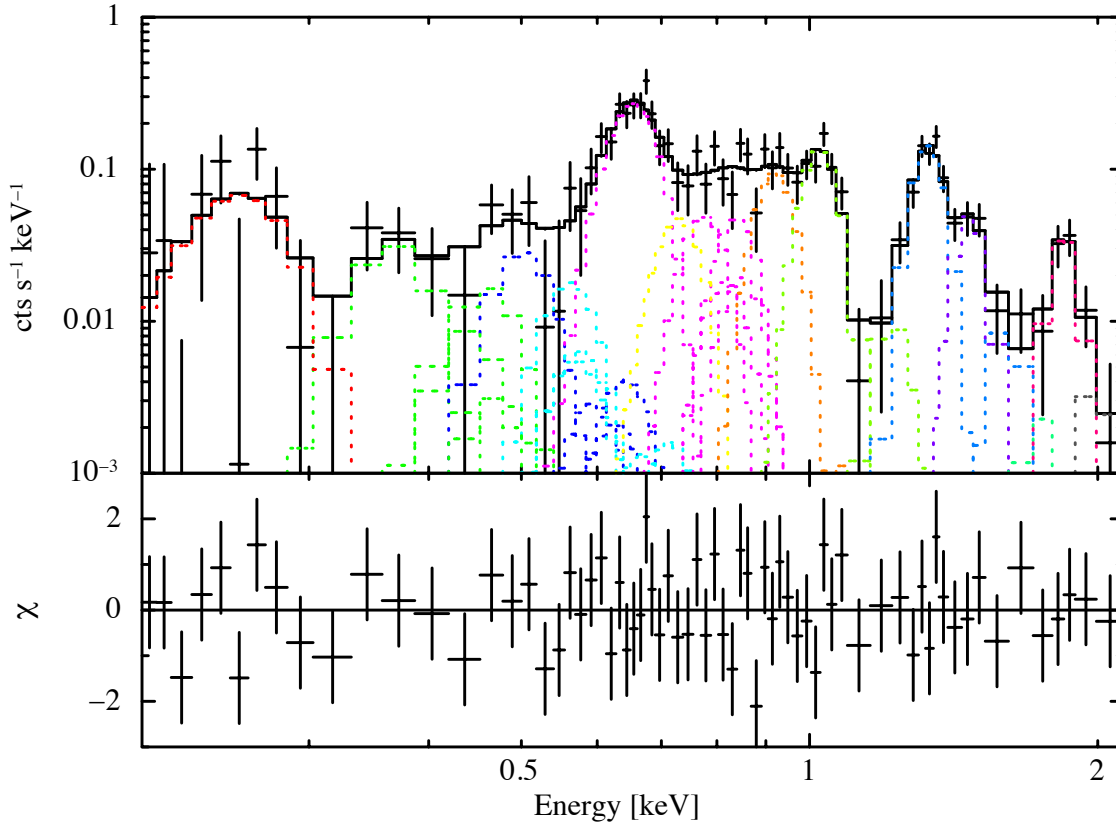


Fig. 7. XIS1 spectrum in the “flare” period. The “stable” spectrum is subtracted as a background. The SWCX model is used and their parameters are listed in table 2. Emission lines are color coded: C VI (green), N VII (blue), O VII (light-blue), O VIII (magenta), Fe XVII (yellow), Ne IX (orange), Ne X (yellow-green), Mg XI (blue-cyan), Mg XII (blue-magenta), Al XIII (green-cyan), Si XIII (red-magenta), and Si XIV (dark-gray).

spectral change during the “flare” period was related to the arrival of the CME.

The spectra during the “pre-flare” and “flare” periods are potentially influenced by the hard continuum originating from particle background (e.g., soft protons as shown in Carter et al. 2010). We checked these spectra after the subtraction of the “stable” period and found no significant excess component in the 2.5–5 keV band. Therefore, the particle continuum was negligible below 2 keV.

5 Time Correlation

The geocoronal SWCX emission is expected to be proportional to the flux of highly charged ions in the solar wind and the column density of neutral atoms in the Earth’s exosphere. The solar wind ion flux is usually replaced with the solar wind proton flux when the solar wind ion to proton abundance

Table 2. Best-fit parameters of the SWCX model shown in figure 7.*

Ion	Principal energy [eV]	Normalization	f_X
C band lines	253 $^{+17}_{-19}$	24 $^{+23}_{-15}$	1.4×10^{-13}
C v	299	–	–
C vi	367	19 ± 9	1.7×10^{-13}
N vi	420	–	–
N vii	500	4.6 ± 3.8	5.8×10^{-14}
O vii	561	5.4 ± 5.0	7.3×10^{-14}
O viii	653	33 ± 3	5.4×10^{-13}
Fe xvii	730	3.4 ± 1.9	5.8×10^{-14}
Fe xvii	820	–	–
Fe xviii	870	–	–
Ne ix	920	4.5 ± 1.1	9.8×10^{-14}
Fe xx	960	–	–
Ne x	1022	5.6 ± 0.9	1.4×10^{-13}
Ne ix	1100	$0.05 (< 0.62)$	1.3×10^{-15}
Ne x	1220	$0.39 (< 0.89)$	1.1×10^{-14}
Mg xi	1330	5.3 ± 0.7	1.7×10^{-13}
Mg xii	1470	1.8 ± 0.5	6.4×10^{-14}
Mg xi	1600	0.50 ± 0.45	1.9×10^{-14}
Al xiii	1730	$0.12 (< 0.58)$	5.0×10^{-15}
Si xiii	1850	1.7 ± 0.5	7.5×10^{-14}
Si xiv	2000	$0.22 (< 0.62)$	1.0×10^{-14}
$\chi^2/\text{d.o.f}$	52.64/53		

* Definitions of parameters are the same as in table 1.

ratio remains constant. This assumption is acceptable for the ambient solar wind, but not for the CMEs. We thus need to refer other information about the solar wind during this observation.

In figure 9, we plot the XIS1 0.52–0.6 keV (O vii) and 0.61–0.69 keV (O viii) light curves and the solar wind proton and alpha fluxes taken from the WIND SWE and ACE SWEPAM data.^{6,7} These solar wind monitoring satellites orbit around the Lagrangian point L_1 between the Sun and Earth. The average positions of the WIND and ACE satellites during this observation were (259, 32) and (223, –12) Earth radii (R_E) in the GSE XY plane, respectively. The solar wind data were not corrected for the traveling time between the L_1 point to the near-Earth. The solar wind proton

⁶ <ftp://spdf.gsfc.nasa.gov/pub/data/wind/swe/>.

⁷ http://www.srl.caltech.edu/ACE/ASC/level2/lvl2DATA_SWEPAM.html.

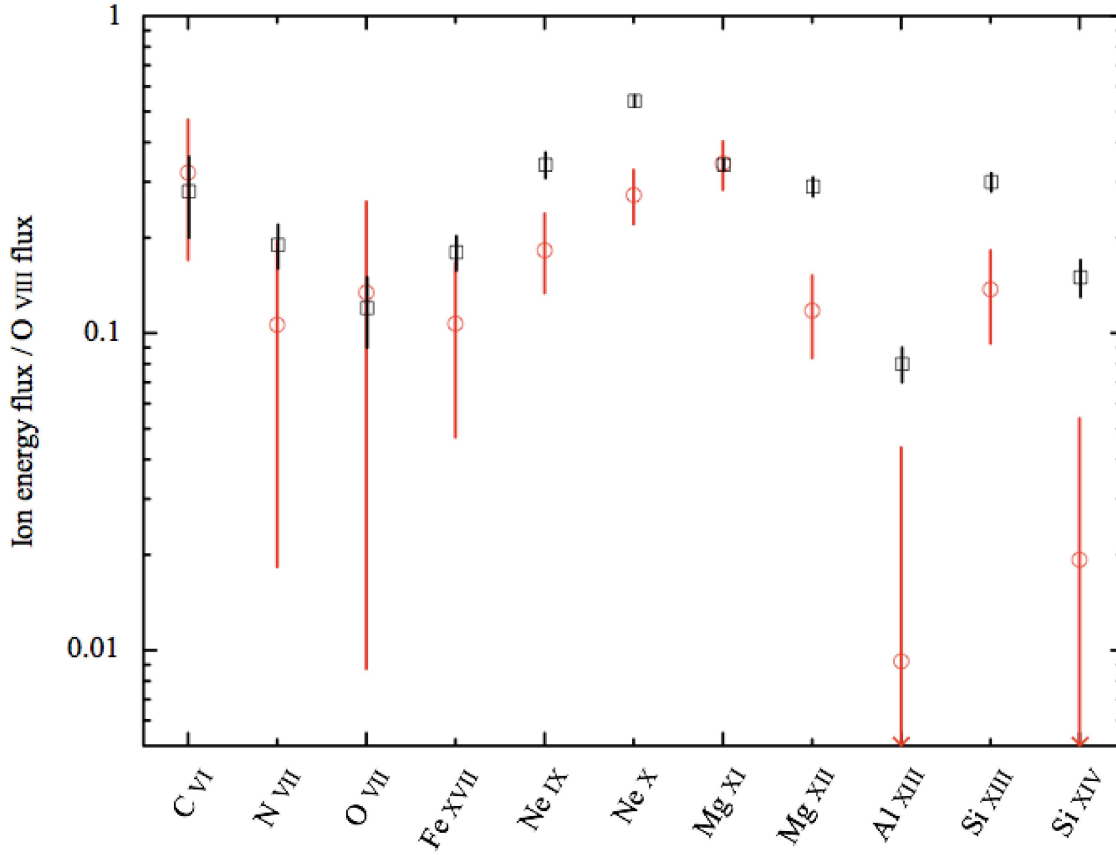


Fig. 8. Line energy flux ratio to the O VIII. Red and black data points indicate the best-fit parameters of this observation and Carter et al. (2010), respectively.

and alpha fluxes suddenly increase just before DOY 104, which corresponds to the arrival of the CME-induced interplanetary shock and the passage of the turbulent sheath. The solar wind proton flux gradually decreases at the arrival of the CME, while the solar wind alpha flux increases again around DOY 104.8. The presence of enhanced alpha particles to proton ratios is rare in the ambient solar wind and typically associated with CMEs (Richardson & Cane 2004). Therefore, the solar wind alpha flux become a good indicator of the geocoronal SWCX events, especially associated with the CMEs.

To check the correlation between the geocoronal SWCX emission and the solar wind alpha flux, we conducted a cross-correlation analysis by using a method described in Ezoe et al. (2010). The ACE data was unavailable during a part of this observation. For this procedure, we binned the O VII and O VIII count rates and the WIND alpha flux into the same time bins of 4096 s. Figure 10 shows the cross correlations between the X-ray light curves and the WIND alpha flux. The correlation

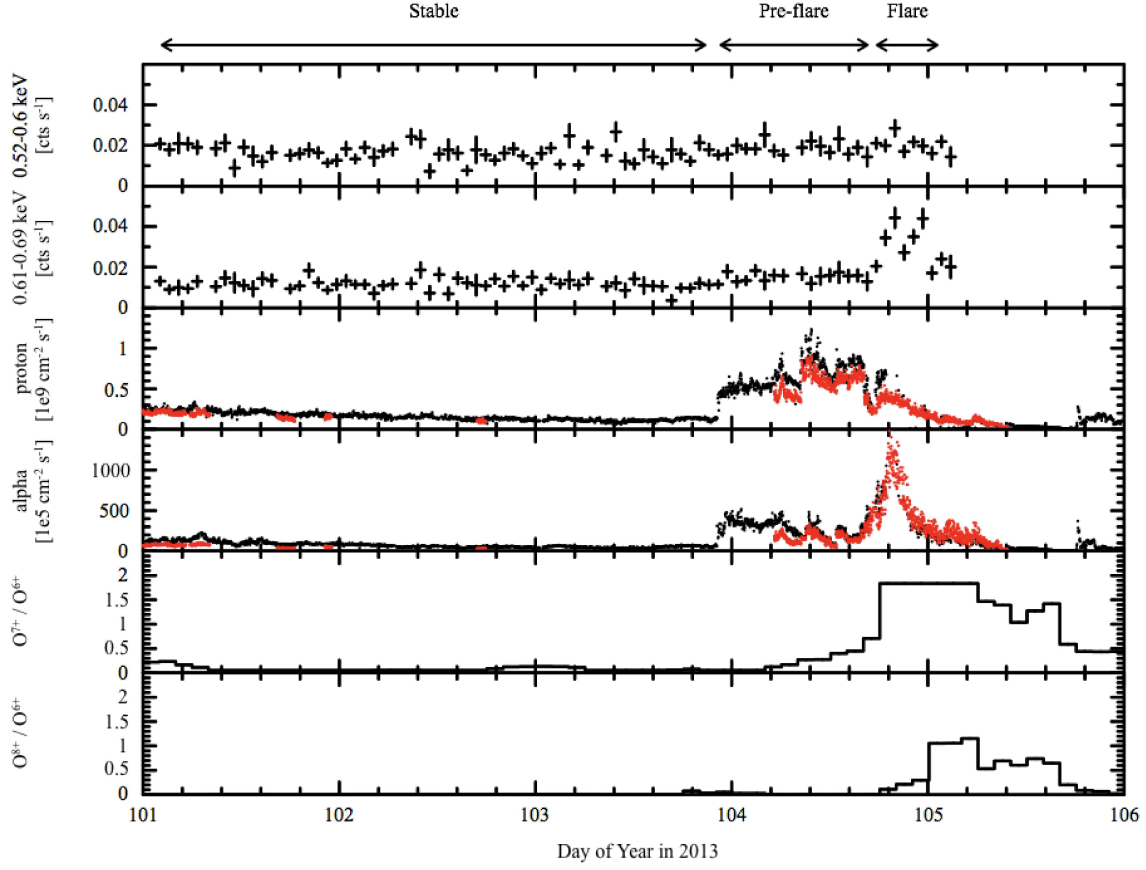


Fig. 9. XIS1 light curves in 0.52–0.6 keV (O VII) and 0.61–0.69 keV (O VIII), solar wind proton flux, solar wind alpha flux, O^{7+}/O^{6+} , and O^{8+}/O^{6+} as function of DOY in 2013. The vertical errors are 1σ significance. The solar wind proton and alpha fluxes were taken from WIND SWE data (black) and ACE SWEFAM data (red). The oxygen ion ratios were taken from ACE SWICS data. The solar wind data are not corrected for the traveling time between the L_1 point to the near-Earth.

coefficients for O VII and O VIII have a weak peak of ~ 0.3 and a strong peak of ~ 0.7 , respectively. These peaks have a time delay of 0–12288 s. The positive value means that the WIND alpha flux has a time delay against the X-ray light curves. The expected time delay was estimated as ~ 3600 s from the distance between the WIND and Suzaku satellites and the average solar wind speed during this observation. We then conducted the same procedure with low-resolution OMNI data time-shifted to the near-Earth.⁸ However, the OMNI alpha flux remained a time delay at 0–8192 s. We also noticed that the time delay for O VIII is slightly shifted to the positive side than that for O VII. These time delay may be due to the solar wind transportation in the magnetosphere and/or the ion distribution within the CME.

⁸ (<https://omniweb.gsfc.nasa.gov/ow.html>).

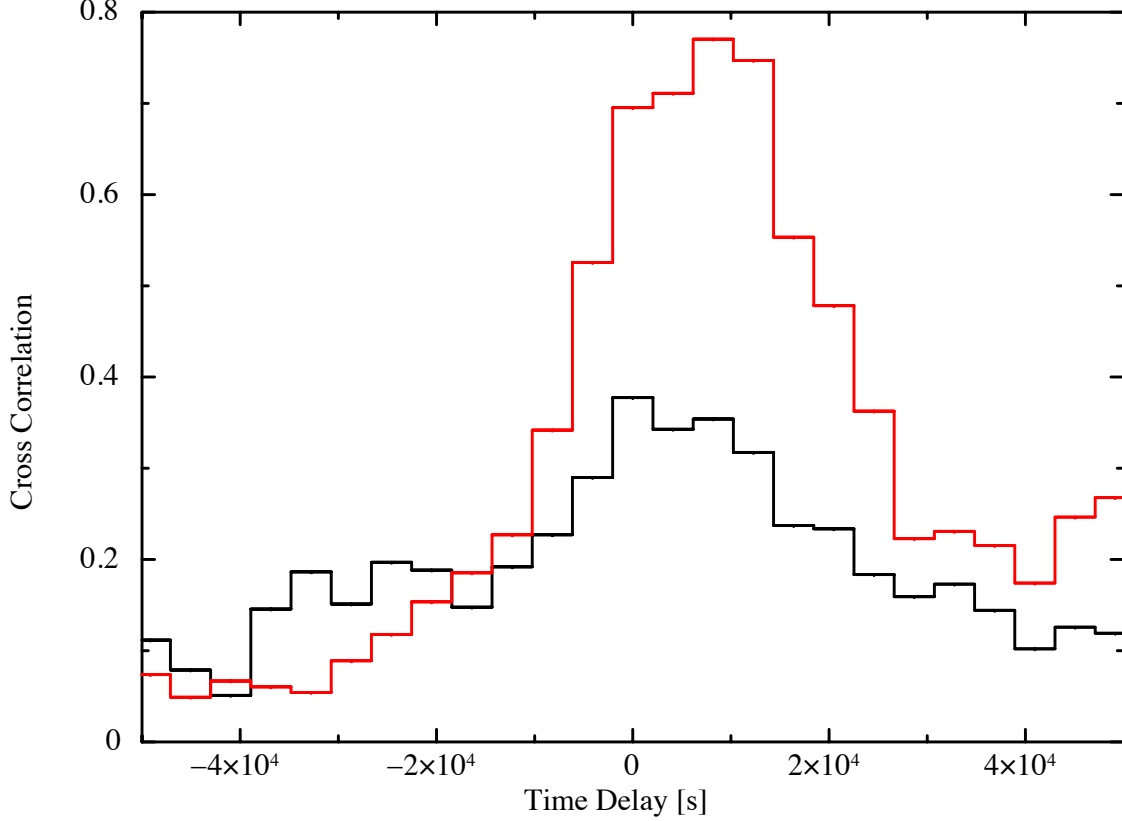


Fig. 10. Cross correlations between the XIS1 light curves and the WIND alpha flux. Black and red bars indicate the 0.52–0.6 keV (O VII) and 0.61–0.69 keV (O VIII) correlation coefficients, respectively. A positive delay means that the WIND data leads the XIS1 count rates.

We simply assumed no time delay and a time delay of 8192 s to the WIND alpha flux corresponding to the O VII and O VIII count rates, respectively. Figure 11 shows the correlations between the O VII and O VIII count rates and the WIND alpha flux considering the above time delay. These correlations are represented by a linear function expressed as

$$C_{\text{XIS}} [\text{cts s}^{-1}] = a \times C_{\text{alpha}} [10^5 \text{ cm}^{-2} \text{ s}^{-1}] + b, \quad (1)$$

where a is the SWCX emissivity and b is an offset emission due to the instrument and sky backgrounds. The O VII best-fit parameters are $a = (1.0 \pm 0.2) \times 10^{-5}$ and $b = (14.6 \pm 0.4) \times 10^{-3}$ with $\chi^2/\text{d.o.f} = 121.24/79$, while the O VIII best-fit ones are $a = (2.5 \pm 0.2) \times 10^{-5}$ and $b = (9.6 \pm 0.4) \times 10^{-3}$ with $\chi^2/\text{d.o.f} = 141.01/79$. From the area of the TDX region and the spectral fitting shown in figure 7, the X-ray count rate is converted into the X-ray flux per solid angle. The emissivity for O VII and O VIII are 0.009 ± 0.002 and 0.030 ± 0.002 LU per $10^5 \text{ cm}^{-2} \text{ s}^{-1}$, where LU is photons

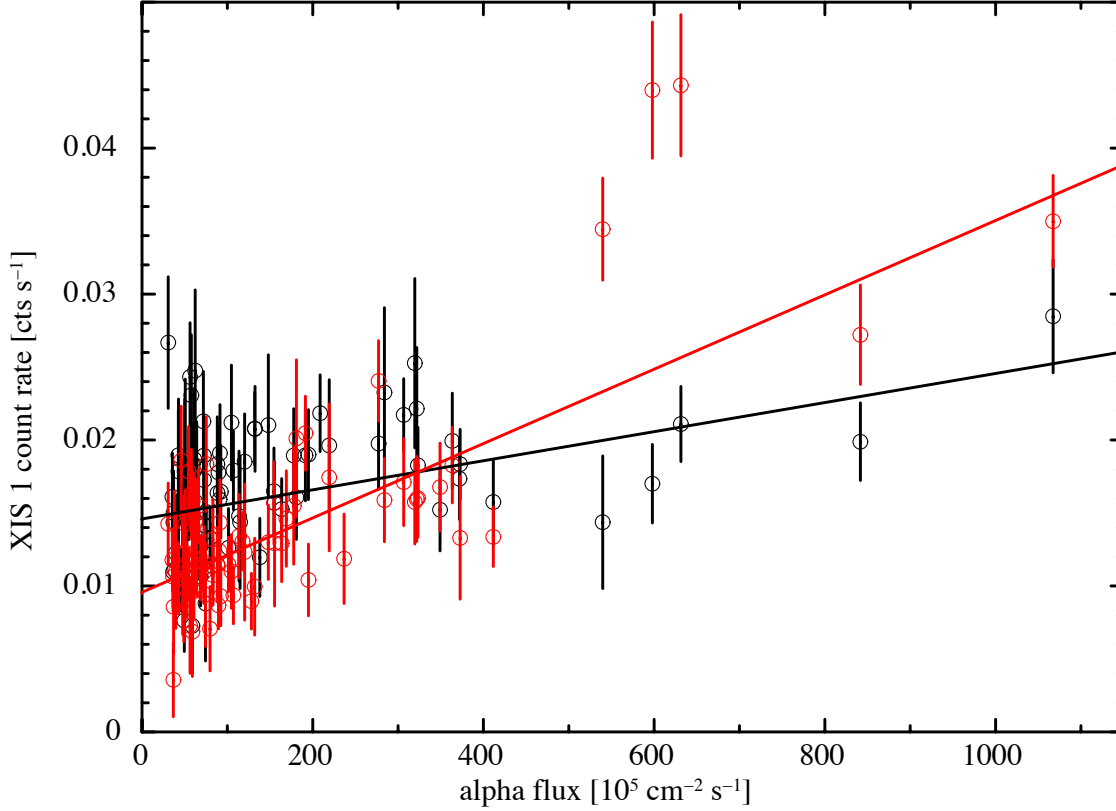


Fig. 11. Correlations between the XIS1 light curves and the WIND alpha flux, considering the no time delay (O VII) and the 8192 s time delay (O VIII). Black and red data points indicate the 0.52–0.6 keV (O VII) and 0.61–0.69 keV (O VIII) count rates, respectively. The vertical errors are 1σ significance. The solid curves are the best-fit linear functions.

$\text{s}^{-1} \text{ cm}^{-2} \text{ str}^{-1}$. The positive intercepts in the O VII and O VIII linear functions are 13.3 ± 0.4 and 11.2 ± 0.4 LU, respectively. This means that there remains a count rate because of the XIS instrumental background and the sky background even if the solar wind alpha flux is zero. The same intercept was observed in our past geocoronal SWCX studies, in which the solar wind proton or ion fluxes were used to derive the coefficients as in Ezoe et al. (2011) and Ishikawa et al. (2013).

In figure 9, we also plot the oxygen ion ratios taken from the ACE SWICS data.⁹ The ion densities of the solar wind are not available after 2011 August 23. The increased alpha particles within the CME are expected to be accompanied by an increase in all the minor ions. The $\text{O}^{7+}/\text{O}^{6+}$ ratio strongly increases at DOY 104.8, while the $\text{O}^{8+}/\text{O}^{6+}$ ratio clearly late increases at DOY105. This supports that there is the time delay between the best O VII and O VIII coefficient peaks shown

⁹ (http://www.srl.caltech.edu/ACE/ASC/level2/lvl2DATA_SWICS_2.0.html).

in figure 10. In addition, the peak of the enhanced O^{8+}/O^{6+} ratio indicates that the beginning of the strong emission lines is probably delayed from the peak of the increased solar wind alpha flux or the arrival of the CME. However, the O VIII count rate begins to increase at DOY 104.8. We then checked the count rates originating from other SWCX emission lines (Ne IX, Ne X, Mg XI, Mg XII, and Si XIII) and found that these count rates also increase at DOY 104.8. We also noticed that the O VIII emission line is prominent even though the O^{8+}/O^{6+} ratio is smaller than the O^{7+}/O^{6+} ratio during the “flare” period. The sparse solar wind data hinders us to investigation a more accurate comparison. Therefore, the enhanced oxygen ion ratio are probably not sufficient to explain the beginning of the soft X-ray enhancement and the geocoronal SWCX flux against the ion abundances during this observation.

6 Conclusion

In this paper, we have investigated the geocoronal SWCX event associated with the CME on 2013 April 14–15 with the Suzaku data, following the same procedure as Ezoe et al. (2011). We divided the data into the “stable”, “pre-flare”, and “flare” periods based on the characteristic features of two X-ray light curves. The 0.5–0.7 keV count rate increased slightly during the “pre-flare” period and by a factor of ~ 2 during the “flare” period. The 2.5–5.0 keV count rate were almost constant during this observation. The spectral change during the “pre-flare” period probably originated from the oxygen emission lines and that during the “flare” period consisted of the series of the emission lines from highly ionized carbon to silicon. The former spectrum could be fitted with the two Gaussian model in 0.5–0.7 keV, while the later one was well represented by the Bodewits’s SWCX model, the single Gaussian model around 0.25 keV, and the eleven Gaussian model above 0.7 keV. The SWCX line flux ratios to O VIII showed a similar tendency to those from XMM-Newton data taken in late 2001 October (Carter et al. 2010). From the solar wind signatures, we concluded that the “pre-flare” period was related to the CME-induced interplanetary shock and the turbulent sheath and the “flare” period was affected by the arrival of the CME. The highly compressed solar wind ions in the turbulent sheath resulted in the soft X-ray enhancement and the highly charged ions within the CME constructed the enriched spectrum. However, the solar wind proton flux showed no significant time correlation. We thus studied the time correlation with the solar wind alpha flux and found a good correlation. The correlations between the O VII and O VIII count rates and the solar wind alpha flux showed a positive correlation well represented by the linear functions. This suggests that the solar wind proton flux is not always a good indicator of the geocoronal SWCX events associated with the CMEs and the solar wind alpha flux should be also investigated when the CME-induced soft X-ray enhancement is detected in astronomical observations.

References

- Bodewits, D., et al. 2007, A&A, 469, 1183
- Burlaga, L., Sittler, E., Mariani, F., & Schwenn, R. 1981, J. Geophys. Res., 86, 6673
- Carter, J. A., & Sembay, S. 2008, A&A, 489, 837
- Carter, J. A., Sembay, S., & Read, A. M. 2010, MNRAS, 402, 867
- Carter, J. A., Sembay, S., & Read, A. M. 2011, A&A, 527, A115
- Cravens, T. E. 2000, ApJ, 532, L153
- Cravens, T. E., Robertson, I. P., & Snowden, S. L. 2001, J. Geophys. Res., 106, 24883
- Ezoe, Y., Ebisawa, K., Yamasaki, N. Y., Mitsuda, K., Yoshitake, H., Terada, N., Miyoshi, Y., & Fujimoto, R. 2010, PASJ, 62, 981
- Ezoe, Y., Miyoshi, Y., Yoshitake, H., Mitsuda, K., Terada, N., Oishi, S., & Ohashi, T. 2011, PASJ, 63, S691
- Fujimoto, R., et al. 2007, PASJ, 59, S133
- Gonzalez, W. D., Joselyn, J. A., Kamide, Y., Kroehl, H. W., Rostoker, G., Tsurutani, B. T., & Vasyliunas, V. M. 1994, J. Geophys. Res., 99, 5771
- Ishikawa, K., Ezoe, Y., Miyoshi, Y., Terada, N., Mitsuda, K., & Ohashi, T. 2013, PASJ, 65, 63
- Koyama, K., et al. 2007, PASJ, 59, S23
- Koutroumpa, D., Acero, F., Lallement, R., Ballet, J., & Kharchenko, V. 2007, A&A, 475, 901
- Mckenzie, D. L., Rugge, H. R., & Charles, P. A. 1982, J. Atmos. Terr. Phys., 44, 499
- Mitsuda, K., et al. 2007, PASJ, 59, S1
- Miyoshi, Y., & Kataoka, R. 2005, Geophys. Res. Lett., 32, L21105
- Priest, E. R., & Forbes, T. G. 2002, A&A Rev., 10, 313
- Richardson, I. G., & Cane, H. V. 2004, J. Geophys. Res., 109, A09104
- Robertson, I. P., Collier, M. R., Cravens, T. E., & Fok, M.-C., 2006, J. Geophys. Res., 111, A12105
- Sekiya, N., Yamasaki, N. Y., Mitsuda, K., & Takei, Y., PASJ Lett., 66, L3
- Snowden, S. L., McCammon, D., Burrows, D. N., & Mendenhall, J. A. 1994, ApJ, 424, 714
- Snowden, S. L., Collier, M. R., & Kuntz, K. D. 2004, ApJ, 610, 1182
- Wargelin, B. J., Markevitch, M., Juda, M., Kharchenko, V., Edger, R., & Dalgarno, A. 2004, ApJ, 607, 596
- Warren, J. S., & Hughes, J. P. 2004, ApJ, 608, 261
- Webb, D. F., & Howard, T. A. 2012, Living Rev. Sol. Phys., 9, 3
- Yamaguchi, H., et al. 2014, ApJ, 785, L27
- Zurbuchen, T. H., & Richardson, I. G. 2006, Space Sci. Rev., 123, 31